



36 method, RMSE decreases by  $39.95 \mu\text{g}/\text{m}^3$ , and the relative deviation reduces by 44.87%.  
37 Moreover, validation at two AERONET sites presents a time series change closer to the  
38 true values, with an R of about 0.80. This study is also a preliminary attempt to combine  
39 model-driven and data-driven models, laying a foundation for further atmospheric  
40 research on optimization methods.

41 **Keywords:** PM<sub>2.5</sub>; Physical approach; Machine learning; Volume-to-extinction ratio;  
42 Fine mode fraction

43

## 44 **1. Introduction**

45 Epidemiological studies have indicated that PM<sub>2.5</sub> (fine particulate matter with an  
46 aerodynamic equivalent diameter no greater than  $2.5 \mu\text{m}$ ) can adversely affect human  
47 health, such as increasing the risk of diabetes and respiratory diseases (Bowe et al.,  
48 2018; Pope III et al., 2002; Xu et al., 2013), and accurate surface PM<sub>2.5</sub> concentration  
49 is the basis of air pollution-health related research. Satellite remote sensing has the  
50 advantages of high resolution and global coverage (Ma et al., 2014; Wu et al., 2020; He  
51 et al., 2022), including variables strongly associated with PM<sub>2.5</sub> such as aerosol optical  
52 depth (AOD). Therefore, it has become a mainstream method for fine particle  
53 estimation (Zhang et al., 2021).

54 There are mainly three satellite-based ways of retrieving PM<sub>2.5</sub>. 1) Chemical transport  
55 models-based method. It calculates a scaling factor  $\eta$  between AOD and PM<sub>2.5</sub>  
56 simulated by atmospheric chemical transport models (CTM) (Lyu et al., 2022) and then  
57 transfers the proportional relationship to satellite AOD data when calculating surface  
58 PM<sub>2.5</sub> concentration (Geng et al., 2015; Van Donkelaar et al., 2006). However, the  
59 assumption of a constant factor between simulated and observed values has large  
60 spatiotemporal limitations. 2) Univariate/Multivariate regression. This kind of method  
61 establishes a statistical model between AOD, auxiliary variables, and ground PM<sub>2.5</sub>  
62 observations. Machine learning is a common tool for such data-driven methods due to  
63 its powerful nonlinear fitting ability between multiple variables (Irrgang et al., 2021).  
64 But the regression is affected by the distribution and density of ground stations (Gupta  
65 and Christopher, 2009; Li et al., 2017). 3) Semi-empirical physical approach. Taking

66 the physical theory as the basis, surface  $PM_{2.5}$  is derived through an empirical formula  
67 constructed from AOD and some PM-related key parameters, including an important  
68 empirical parameter related to the optical properties (S). The process steps are explicit  
69 and independent of ground station observations. Meanwhile, this approach has stronger  
70 physical interpretability than the previous two methods with a large space for  
71 optimization.

72 Due to the complexity of the physical parameters, many studies have optimized the  
73 semi-empirical physical approach. Based on 355nm-band radar observations, Raut and  
74 Chazette (2009) introduced a specific extinction cross-section to simplify the  
75 expression of S and  $PM_{2.5}$  concentration was estimated. Kokhanovsky et al. (2009)  
76 constructed a particle-effective radius model, which can obtain the particle  
77 concentrations throughout the atmospheric column. Furthermore, Zhang and Li (2015)  
78 proposed the physical  $PM_{2.5}$  remote sensing method (PMRS). It replaced S by defining  
79 a volume-to-extinction ratio of fine particles ( $VE_f$ ) and used a quadratic polynomial of  
80 fine mode fraction (FMF) to simulate  $VE_f$ , showing certain advantages (Li et al., 2016;  
81 Zhang et al., 2020).

82 However, the above semi-physical empirical models have some shortcomings. Firstly,  
83 the satellite data used in the models are blocked by clouds and fog in some areas, thus  
84 high-coverage and high-precision products need to be excavated and applied; secondly,  
85 there are still large uncertainties in estimating physical parameters (such as a simple  
86 polynomial fit to S in the PMRS method) and their expressions need to be improved.  
87 To date, machine learning (ML) has developed rapidly (He et al., 2021). It can detect  
88 complex nonlinear relationships of multiple data and model their interaction (Yuan et  
89 al., 2020; Lee et al., 2022). This provides an idea for improving the accuracy of physical  
90 parameter acquisition, so as to estimate high-precision  $PM_{2.5}$  through semi-physical  
91 empirical models.

92 According to this idea, our study proposes an optimized semi-empirical physical  
93 model (RF-PMRS) based on the PMRS theory, which attempts to explore the possibility  
94 of combining physical models and ML. To be specific, we creatively embed ML (the  
95 random forest model) into the PMRS method to simulate the physical parameter (i.e.,

96  $VE_f$ ) derived from FMF and related variables, thus optimizing the previous polynomial  
 97 expression. Besides, to further improve the  $PM_{2.5}$  retrieval accuracy, the physical-deep  
 98 learning FMF (Phy-DL FMF) dataset generated by a hybrid retrieval algorithm of ML  
 99 and physical mechanisms is introduced. Ultimately, we comprehensively validate the  
 100 performance of the  $PM_{2.5}$  obtained by our optimized approach.

101 The remained part of our article is as follows. Section 2 describes the experimental  
 102 datasets. Section 3 illustrates the specific derivation process of the proposed method.  
 103 Section 4 analyzes the evaluation results. Some supporting experiments are discussed  
 104 in section 5. And the final part provides the conclusion.

105

## 106 **2. Data**

### 107 **2.1. AERONET data**

108 The Aerosol Robotic Network (AERONET) is a federation of ground-based sun-sky  
 109 radiometer networks, providing worldwide remote sensing aerosol data for more than  
 110 25 years (Holben et al., 1998). Until now, the Version 3 dataset has been released (Giles  
 111 et al., 2017). Due to its high quality, the data from AERONET have been regarded as  
 112 theoretical true values to evaluate satellite-based products in related studies (Chen et  
 113 al., 2020; Gao et al., 2016; Wang et al., 2019). AOD, FMF, and Volume Size  
 114 Distribution products with Level 2.0 (quality-assured) are applied to calculate the true  
 115 values of the physical parameters, and then to implement our modeling purpose (not  
 116 involved in  $PM_{2.5}$  calculations). A total of 9 AERONET sites corresponding to four  
 117 typical aerosol types participate in the training. Table 1 shows the specific information.

118

119 **Table 1.** Data information of 9 AERONET sites classified by aerosol types. Location indicates the  
 120 latitude and longitude, where ‘-’ means the south latitude and west longitude. Two sites in bold fonts  
 121 participate in the  $PM_{2.5}$  validation experiment.

Aerosol Type	Site	Location (LAT, LON)	Training period	Isolated- validation period
	<b>Beijing</b>	<b>39.98°, 116.38°</b>	2001-2017	2018-2019
<b>Urban- industrial</b>	<b>Beijing-CAMS</b>	<b>39.93°, 116.32°</b>	2012-2017	2018-2019
	XiangHe	39.75°, 116.96°	2004-2017	/
	Ascension Island	-7.98°, -14.41°	2010-2017	2018-2019

	Capo Verde	16.73°, -22.94°	2010-2017	2018
<b>Biomass burning</b>	CUIABA	-15.73°, -56.07°	2010-2017	2018-2019
	MIRANDA			
<b>Desert dust</b>	GSFC	38.99°, -76.84°	2010-2017	2018-2019
	Mexico City	19.33°, -99.18°	2010-2017	/
<b>Oceanic</b>	Solar Village	24.91°, 46.40°	2010-2013	/

122

## 123 **2.2. MODIS AOD**

124 MCD19A2, the Moderate-resolution Imaging Spectroradiometer (MODIS) C6  
125 Level-2 gridded (L2G) land AOD product (Lyapustin and Wang, 2015), is selected in  
126 this study. It is derived from the Multi-Angle Implementation of the Atmospheric  
127 Correction (MAIAC) algorithm, which can improve the accuracy in cloud detection  
128 and aerosol retrieval (Lyapustin et al., 2011). Besides, this new advanced algorithm  
129 jointly combines MODIS Terra and Aqua into a single sensor (Lyapustin et al., 2014).  
130 The product is produced daily with a 1km resolution, including aerosol parameters such  
131 as 470nm/550nm AOD, quality assurance (QA), and uncertainty factors.

132 The processing of MCD19A2 data (HDF format) is mainly divided into five steps:  
133 AOD/QA band extraction, best quality AOD selection, Terra/Aqua data synthesis,  
134 missing information reconstruction, and mosaic. Finally, the daily AOD distribution in  
135 GeoTiff format is obtained.

136

## 137 **2.3. Phy-DL FMF dataset**

138 The original global land FMF products have poor data integrity and low accuracy.  
139 To enhance their reliability, Yan et al. (2022) have released a satellite-based dataset  
140 called Phy-DL FMF, which integrates physical and deep learning methods. Specifically,  
141 it selects the FMF data obtained by a physical method (i.e., Look-Up-Table-based  
142 Spectral Deconvolution Algorithm, LUT-SDA) as the optimization target (Yan et al.,  
143 2017). Then it combines the Phy-based FMF into a deep-learning model along with  
144 multiple auxiliary data such as satellite observations for the final Phy-DL results. Note  
145 that the process is trained with AERONET data as the ground truth. The product has a  
146 spatial resolution of 1° and covers from 2001 to 2020 (daily scale). In the comparison

147 experiment against the ground FMF, Phy-DL FMF shows a higher accuracy ( $R = 0.78$ ,  
148  $RMSE = 0.100$ ) than MODIS FMF ( $R = 0.37$ ,  $RMSE = 0.282$ ) (Yan et al., 2022).

149

#### 150 **2.4. Meteorological data**

151 The meteorological data are obtained from the ERA5 dataset, including the values of  
152 planetary boundary layer height (PBLH) and relative humidity (RH). As the fifth-  
153 generation reanalysis product released by the European Center for Medium-Range  
154 Weather Forecasts (ECMWF), ERA5 provides atmospheric data at  $0.25^\circ$  every hour  
155 based on the data assimilation principle (Hersbach et al., 2018). It should be noted that  
156 RH is not archived directly in ERA5, thus should be calculated by 2m temperature  $T$   
157 and dew point temperature  $T_d$  (referred to ERA-Interim: documentation).

$$158 \quad RH = 100 \times \frac{e_s(T_d)}{e_s(T)} \quad (1)$$

159 Here,  $e_s(t)$  represents the saturation vapor pressure related to a Celsius temperature  $t$   
160 (Simmons et al., 1999).

$$161 \quad e_s(t) = 6.112 \times \exp\left(\frac{17.67 \times t}{t + 243.5}\right) \quad (2)$$

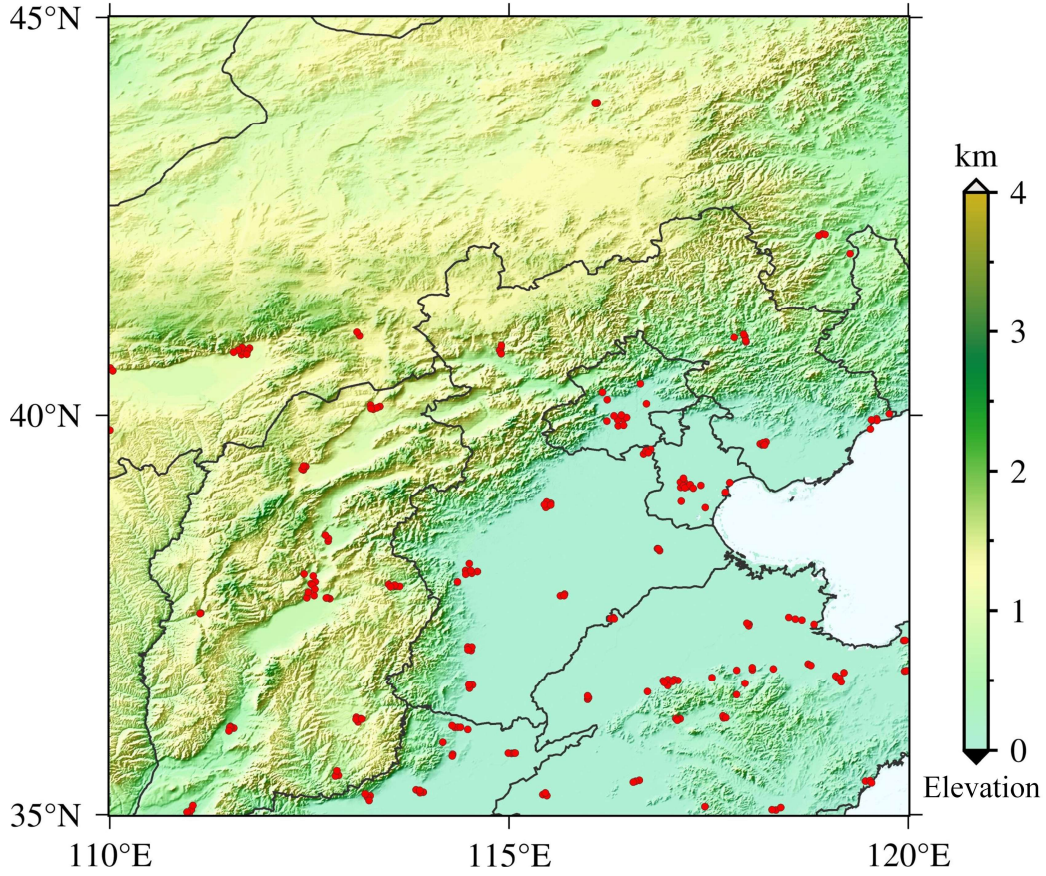
162

#### 163 **2.5. Ground PM<sub>2.5</sub> measurements**

164 The North China Region (NC) is chosen as the main experimental validation area for  
165 the final PM<sub>2.5</sub> calculations. The near-surface hourly PM<sub>2.5</sub> values are obtained from the  
166 China National Environmental Monitoring Center (CNEMC). Nowadays, over 1600  
167 ground-based monitors are working continuously and a total of 232 stations (in 2017)  
168 participate in this work. Fig. 1 displays the site distributions of the NC region.

169

## The location of NC stations



170 110°E 115°E 120°E  
171 **Fig. 1.** The location of ground stations in the NC region (35°-45°N, 110°-120°E). The red points  
172 represent NC stations.

### 173 174 **3. Methods**

175 Based on the basic physical properties of atmospheric aerosols, the semi-physical  
176 empirical approach starts from the integration of PM mass concentration and AOD.  
177 Then it combines several key factors related to  $PM_{2.5}$ , to derive the in situ  $PM_{2.5}$   
178 concentration through multiple remote sensing variables (Koelemeijer et al., 2006). The  
179 overall empirical relationship can be represented as:

$$180 \quad PM_{2.5} = AOD \frac{\rho}{H \cdot f(RH)} S \quad (3)$$

181 where  $\rho$  denotes the particle density and  $H$  denotes the atmospheric boundary layer  
182 height.  $f(RH)$  represents the hygroscopic growth factor related to relative humidity  
183 ( $RH$ ).  $S$  is an optical characteristic parameter that should be simulated.

184

### 185 3.1. PMRS method

#### 186 3.1.1. The expression of $VE_f$

187 To illustrate S more precisely, PMRS defines the columnar volume-to-extinction ratio  
188 of fine particles (i.e.,  $VE_f$ ), which can be regarded as the basis of our optimization  
189 method. So equation (3) is transformed into:

$$190 \quad PM_{2.5} = AOD \frac{\rho}{H \cdot f(RH)} VE_f \quad (4)$$

191 Related to particle size, aerosol extinction, and other properties,  $VE_f$  can be expressed  
192 as:

$$193 \quad VE_f = \frac{V_{f,column}}{AOD_f} \quad (5)$$

$$194 \quad AOD_f = AOD \cdot FMF \quad (6)$$

195 Here,  $AOD_f$  is the fine particle AOD and  $FMF$  is the fine mode fraction.  $V_{f,column}$   
196 can be expressed by the vertical integral of particle volume size distributions (PVSD)  
197 within a certain aerodynamic diameter range:

$$198 \quad V_{f,column} = \int_0^{D_{p,c}} V(D_p) dD_p \quad (7)$$

199  $D_{p,c}$  represents the cutting diameter, and the empirical value of  $2.0 \mu\text{m}$  is chosen based  
200 on previous literature (Hand and Kreidenweis, 2002; Hänel and Thudium, 1977). And  
201  $V(D_p)$  represents the PVSD corresponding to the geometric equivalent diameter ( $D_p$ ).

202

#### 203 3.1.2. Specific process and limitations

204 The PMRS method is developed from equation (4). Based on satellite AOD, the near-  
205 surface  $PM_{2.5}$  can be obtained through multi-step transformation. Fig. 2(a) shows its  
206 specific process. Each arrow refers to a step, respectively: size cutting (output:  $AOD_f$ ),  
207 volume visualization (output:  $V_{f,column}$ ), bottom isolation (output:  $V_f$ , fine particle volume  
208 near the ground), particle drying (output:  $V_{f,dry}$ , dry  $V_f$ ) and  $PM_{2.5}$  weighting. The  
209 overall expression is as follows:

$$210 \quad PM_{2.5} = AOD \frac{FMF \cdot VE_f \cdot \rho_{f,dry}}{PBLH \cdot f_0(RH)} \quad (8)$$

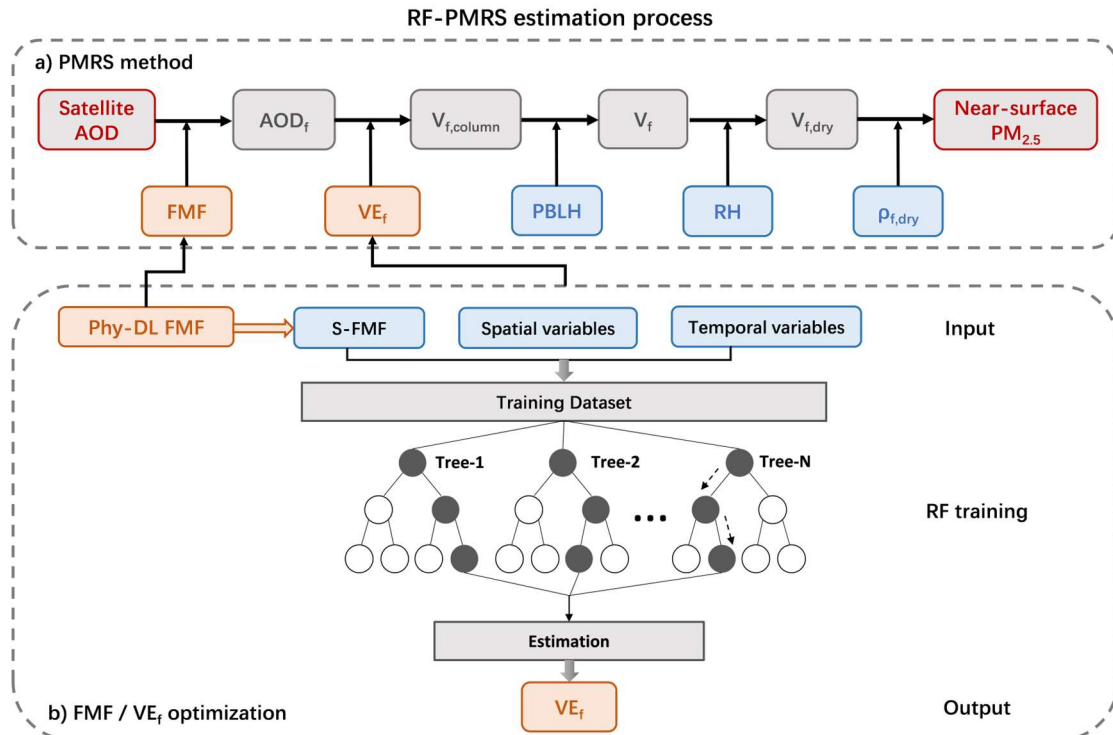


211 
$$f_0(RH) = \left(1 - \frac{RH}{100}\right)^{-1} \quad (9)$$

212 where  $FMF$  denotes the fine mode fraction,  $\rho_{f,dry}$  denotes the dry mass density of  
 213  $PM_{2.5}$ , and  $PBLH$  represents the planet boundary layer height.  $f_0(RH)$  represents  
 214 the approximation of  $f(RH)$  in equation (4), as expressed in equation (9).  
 215 Considering the aerosol types in different regions, PMRS fits  $VE_f$  to a quadratic  
 216 polynomial relation of  $FMF$  (Zhang and Li, 2015):

217 
$$VE_f = 0.2887FMF^2 - 0.4663FMF + 0.356 \quad (0.1 \leq FMF \leq 1.0) \quad (10)$$

218



219 **Fig. 2.** Surface  $PM_{2.5}$  estimation flow of RF-PMRS. a) The five steps of the PMRS method. Gray  
 220 boxes are the intermediate outputs, blue boxes are the input data, and orange ones denote the  
 221 variables to be optimized. b) The specific optimization of RF-PMRS:  $FMF$  dataset replacement and  
 222  $VE_f$  simulation by RF model.  
 223  
 224

225 PMRS has strong physical significance, the calculation steps are well-defined and  
 226 site-independent. Zhang and Li (2015) tested the performance of PMRS on 15 stations,  
 227 and the validation results had an uncertainty of 34%. Compared with the ground value  
 228 of Jinhua city in China, a 31.3% relative error was generated in Li et al. (2016). Besides,  
 229 Zhang et al. (2020) applied it to the  $PM_{2.5}$  change analysis and prediction experiments  
 230 in China over 20 years. However, there may be a more complex nonlinear relationship

231 between  $VE_f$  with FMF, not just a simple quadratic formula. Since  $VE_f$  is related to the  
232 aerosol type, adding other spatiotemporal variables may optimize the fitting process.  
233 Additionally, high-quality FMF data is the basic guarantee for the estimated  $PM_{2.5}$   
234 quality. In a word, to further improve the physical method, a better nonlinear model  
235 between  $VE_f$  and related variables from reliable datasets needs to be explored.

236

### 237 **3.2. Optimization method: RF-PMRS**

238 Therefore, to overcome the above disadvantages, an optimized method called RF-  
239 PMRS is proposed. Fig. 2(b) shows the process of our method, while optimizations for  
240 FMF and  $VE_f$  are described separately below.

#### 241 **1) FMF dataset selection**

242 We introduce the Phy-DL FMF dataset into the PMRS method to improve the  
243 accuracy of size-cutting results. In terms of performance, it exhibits higher accuracy  
244 and wider space-time coverage than satellite products (Yan, 2021). See the data section  
245 for details.

246

#### 247 **2) $VE_f$ simulation based on ML**

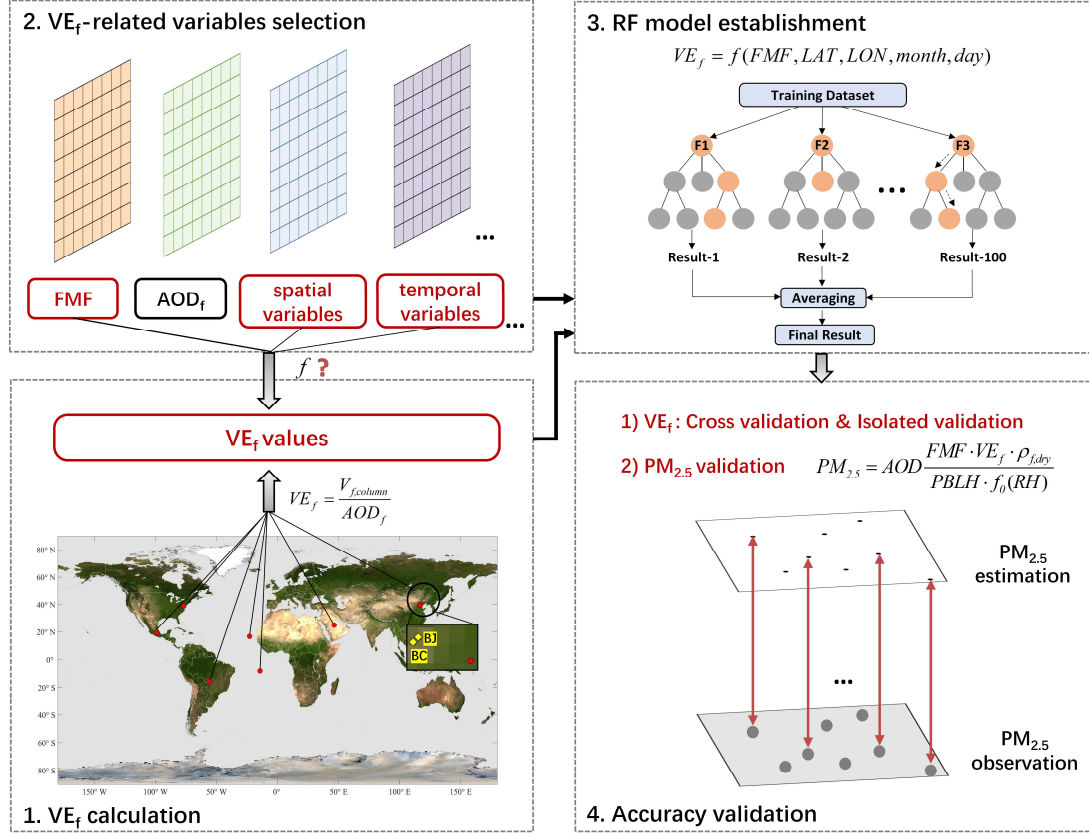
248 The main idea is to establish an ML model between the  $VE_f$  truth obtained from  
249 multiple AERONET sites and related variables, thus improving the subsequent  $VE_f$ -  
250 simulation accuracy (Fig. 3).

251

#### 252 **Step 1 $VE_f$ calculation**

253 The  $VE_f$  true values are calculated concerning equations (5)-(7). Due to the  
254 spatiotemporal variability of different aerosol types, we calculate the  $VE_f$  values at 9  
255 AERONET stations around the world (Table 1) to train a universal model. The first step  
256 in Fig. 3 shows their distribution characteristics. Among them, Beijing and Beijing-  
257 CAMS sites are highlighted since they participate in the subsequent point validation  
258 experiment.

259



260

261 **Fig. 3.** Specific steps for simulating  $VE_f$  based on ML in our RF-PMRS method. The map used in  
 262 step 1 is from NASA Visible Earth ([https://visibleearth.nasa.gov/images/57752/blue-marble-land-](https://visibleearth.nasa.gov/images/57752/blue-marble-land-surface-shallow-water-and-shaded-topography)  
 263 [surface-shallow-water-and-shaded-topography](https://visibleearth.nasa.gov/images/57752/blue-marble-land-surface-shallow-water-and-shaded-topography)). The red points in step 1 represent the distribution  
 264 of the 9 AERONET sites and the two yellow quadrangles in the zoom-in view highlight the Beijing  
 265 (BJ) and Beijing-CAMS (BC) sites.

## 266 Step 2 $VE_f$ -related variables selection

267 According to the theory, FMF is selected as the most important modeling variable.  
 268 Previous studies have also shown that the FMF- $VE_f$  relationship has a good single-  
 269 value correspondence, which is not affected by AOD. Compared with  $AOD_f$  and  
 270  $V_{f,column}$ , FMF is a better indicator for estimation (Zhang and Li, 2015). In addition,  
 271 considering the spatiotemporal heterogeneity of  $VE_f$ , the latitude, longitude (LAT,  
 272 LON), and data time (month, day) of each site are added to the training.

273

## 274 Step 3 RF model establishment

275 From step 2,  $VE_f$  can be expressed as:

$$276 \quad VE_f = f(FMF, LAT, LON, month, day) \quad (11)$$

277 We optimize  $VE_f$  expression based on random forest (RF). RF is made up of multiple  
278 decision trees that can build high-accuracy models based on fewer variables (Svetnik  
279 et al., 2003; Yang et al., 2020). This ensemble ML method randomly samples the  
280 training dataset to form multiple subsets and random combinations of features are  
281 selected in node splitting (Belgiu and Drăguț, 2016). The specific process is to 1)  
282 generate training subsets, 2) build an optimal model, and 3) calculate the result (Fig. 3  
283 shows its flowchart). Note that the station FMF values (S-FMF) are used when training.

284

#### 285 **Step 4 Accuracy validation**

286 The  $VE_f$  estimation is also based on equation (11), where  $f$  is the optimal relationship  
287 after RF parameter adjustment, and Phy-DL FMF is applied to realize the extension of  
288 model results from point to surface. 10-fold cross-validation (CV) (Rodriguez et al.,  
289 2009) and isolated-validation (IV) are used to evaluate model performance (For details  
290 of the validation methods, see Appendix A1).

291

#### 292 **3) PM<sub>2.5</sub> value estimation and evaluation**

293 Then, calculate  $PM_{2.5}$  according to the corresponding process (equation (8)). The  
294 variables (in sections 2.2 to 2.4) are spatially matched to ground sites at their respective  
295 resolutions. And based on UTC, the  $PM_{2.5}$  validation is conducted on a daily scale in  
296 2017. Because of the effective quantity of the AERONET public dataset and MODIS  
297 data, we choose 2017 as the representative year. Note that we select the measured  
298 empirical value of  $\rho_{f,dry}$  (i.e.,  $1.5 \text{ g/cm}^3$ ) for the NC region from Gao et al. (2007).

299 The statistical indicators used in the evaluation include correlation coefficient (R),  
300 mean bias (MB), relative mean bias (RMB), root mean square error (RMSE), and mean  
301 absolute error (MAE). In addition, relative predictive error (RPE) is added to validate  
302 the accuracy of the RF-based  $VE_f$  model. See Appendix A2 for the specific information  
303 on these indicators.

304

#### 305 **4. Experiment results**

306 Three main experiments are conducted to verify the proposed RF-PMRS method,

307 and the specific information is shown in Table 2.

308 **Table 2.** A brief information summary of the experiments conducted in our study.

Experiment	Object	Region	Period	Time scale
Model performance for training $VE_f$	$VE_f$	Global scale (Nine AERONET sites)	CV: Training period in Table 1 IV: Isolated-validation period in Table 1 (See Appendix A1)	Daily
Accuracy evaluation of PMRS/RF-PMRS	$PM_{2.5}$	Two AERONET Sites: Beijing, Beijing-CAMS	2017	Daily
Generalization performance of RF-PMRS	$PM_{2.5}$	North China region	2017	Daily

309

#### 310 **4.1. RF model performance for training $VE_f$**

311 The simulation model of  $VE_f$  is trained based on the data in Table 1 and see Appendix  
 312 A3 for the adjustment of the model parameters. Table 3 shows that RF can capture the  
 313 complex relationship between  $VE_f$  and related variables well. R is as high as 0.974  
 314 (0.975), RMSE and MAE are both small, and RPE is around 30%, which suggests the  
 315 desired estimation accuracy. Overall, the CV results represent the great performance of  
 316 the RF model for extracting information, that is, the relationship of multi-source data  
 317 to  $VE_f$ . In the meantime, the statistical results in CV and IV experiments are similar,  
 318 indicating that the RF model has no obvious overfitting phenomenon.

319

320 **Table 3.** Performance statistics of the RF model for training  $VE_f$ . N represents the number of data,  
 321 and  $VE_f$  has no unit.

	R	RMSE	RPE	MAE	N
<b>Cross-validation (CV)</b>	0.974	0.076	32.9%	0.034	6463
<b>Isolated-validation (IV)</b>	0.975	0.067	29.8%	0.037	814

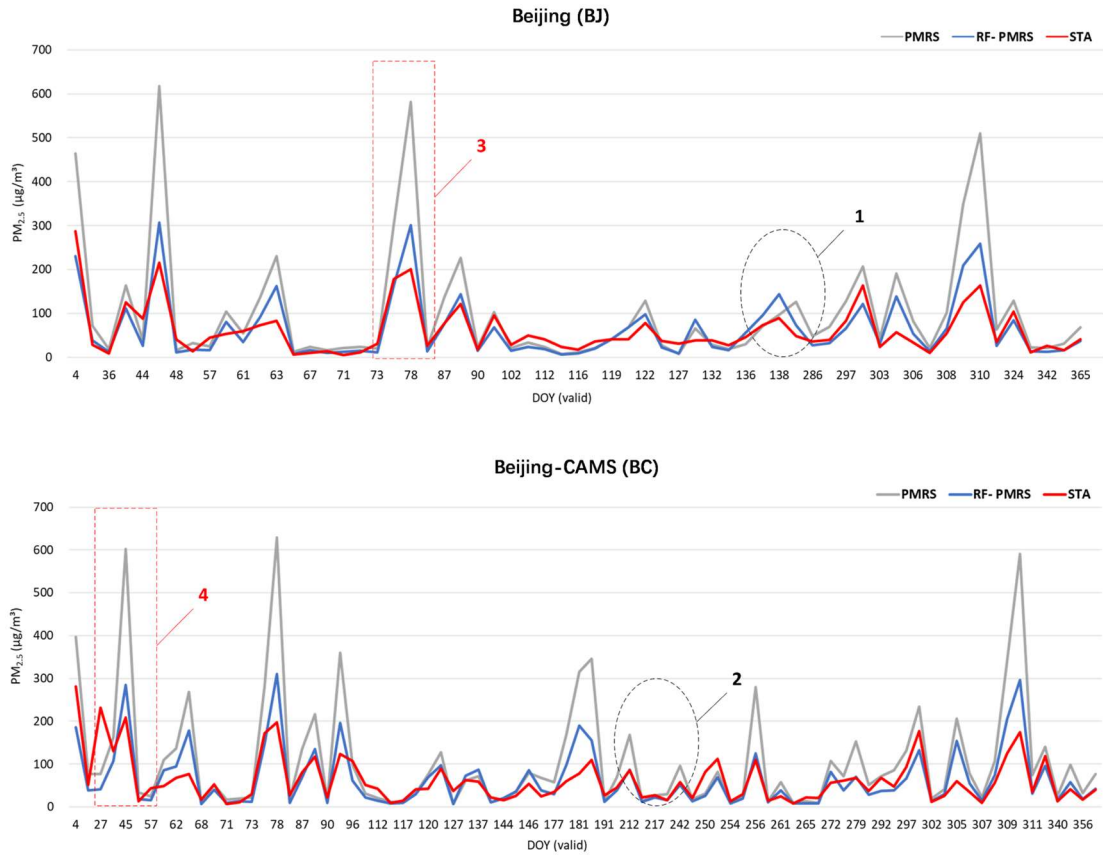
322

#### 323 **4.2. Accuracy evaluation of PMRS/RF-PMRS at AERONET stations**

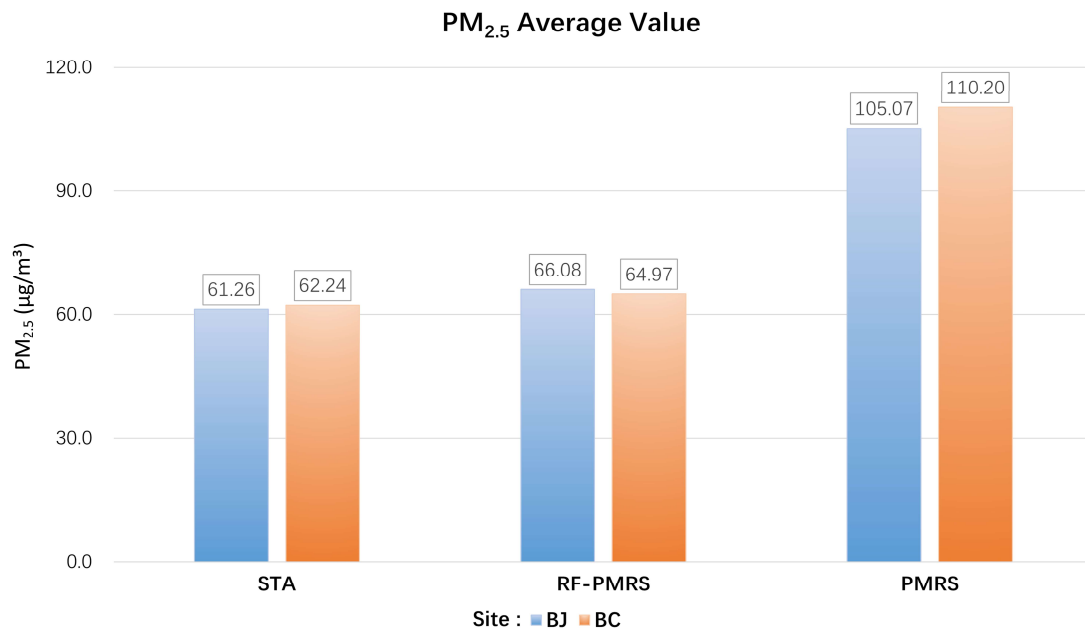
324 After applying the Phy-DL FMF data to the calculation process, the experiment  
 325 compares  $PM_{2.5}$  results of PMRS and RF-PMRS at Beijing (BJ) and Beijing-CAMS  
 326 (BC) AERONET sites in 2017. Here, RF-PMRS simulates  $VE_f$  based on RF, replacing  
 327 the polynomial of the PMRS method. Note that the results of the two sites are compared

328 with their respective nearest ground PM<sub>2.5</sub> stations (distances of 3.64 km and 3.91 km,  
329 respectively, in line with the representative range of ground stations in previous studies  
330 (Shi et al., 2018)).

331 Fig. 4 displays the time series of PM<sub>2.5</sub> values for different models at two sites. The  
332 blue line fits the red line better than the gray one, confirming that the PM<sub>2.5</sub> results of  
333 RF-PMRS are closer to the true values. Within the range of the black circles at positions  
334 1 and 2, the variation of RF-PMRS results has better consistency with the ground truth,  
335 while the PMRS results show dislocation and excessive growth. The overall  
336 performance of the RF-PMRS estimations can signify the effectiveness of our proposed  
337 method framework. As observed in the red boxes at positions 3 and 4, both models have  
338 a certain degree of deviation, which is found to be consistent with the time regularity  
339 of the AOD high values. Meanwhile, Fig. B1 (in Appendix B) plots the bias time series  
340 between PMRS/RF-PMRS and in-situ values. As can be seen, the bias of the  
341 optimization method (RF-PMRS) is stably distributed around zero, which greatly  
342 reduces the numerical uncertainty. And it is worth noting that our method has well  
343 mitigated the apparent overestimation of the original model (PMRS) in the case of  
344 above-normal aerosol loadings. Furthermore, the average PM<sub>2.5</sub> values from ground  
345 stations, PMRS, and RF-PMRS are compared. As for the two sites, the RF-PMRS  
346 results are satisfactory. As depicted in Fig. 5, the RF-PMRS and station mean values  
347 are close, with a difference of 4.82 μg/m<sup>3</sup> (BJ) and 2.73 μg/m<sup>3</sup> (BC), suggesting a good  
348 estimation. Nevertheless, the PMRS results have deviations greater than 40 μg/m<sup>3</sup>, and  
349 overestimation exists at both sites. It can be inferred that, in our proposed method, the  
350 optimization of VE<sub>f</sub> can greatly improve the PM<sub>2.5</sub> estimation accuracy.

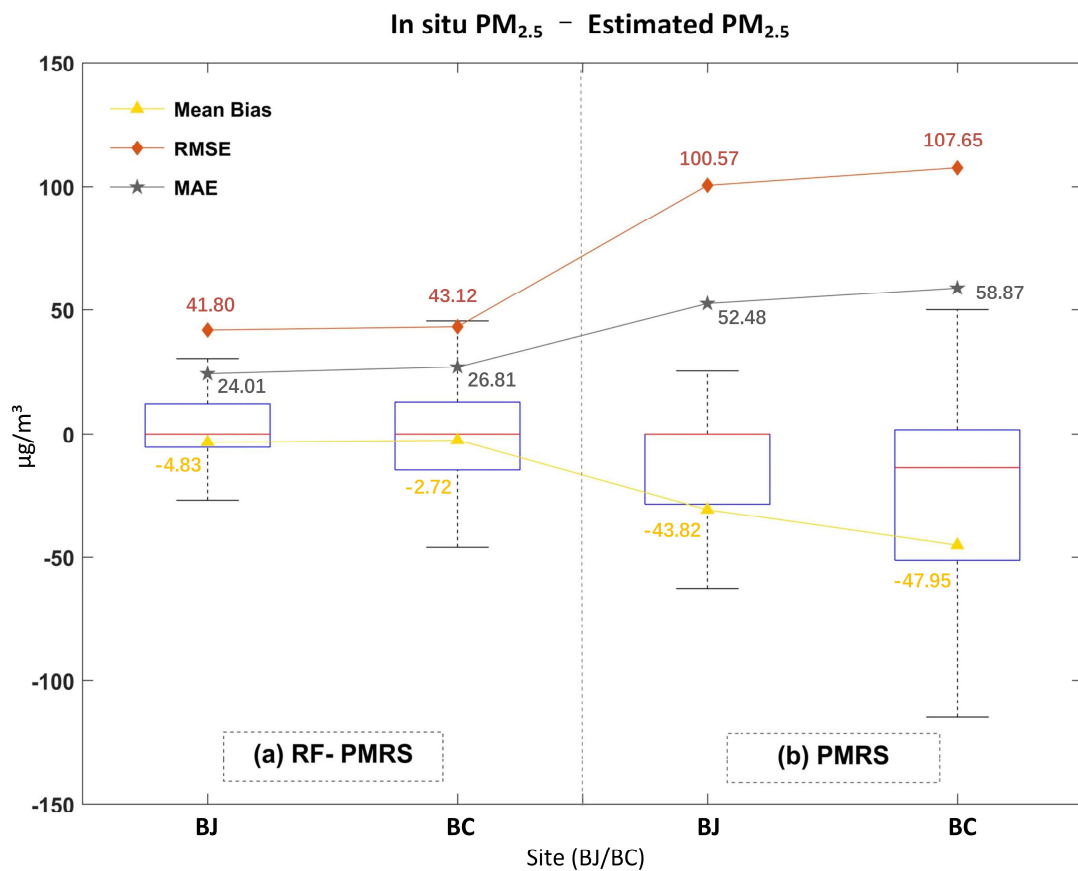


351  
 352 **Fig. 4.** Three PM<sub>2.5</sub> time series at the Beijing (BJ) and Beijing-CAMS (BC) sites under their  
 353 respective DOYs in 2017. Here, DOY (valid) means the day of the year with valid AOD, FMF, and  
 354 other PM<sub>2.5</sub>-related data. Grey, blue, and red lines represent PM<sub>2.5</sub> values of PMRS, RF-PMRS, and  
 355 stations (STA), respectively. The red boxes and black circles select a specific period for analysis.  
 356



357  
 358 **Fig. 5.** Annual average PM<sub>2.5</sub> values from stations (left), RF-PMRS (middle), and PMRS model  
 359 (right) at the BJ and BC sites.

360 Aiming at visually comparing the optimization effect, Fig. 6 plots the PM<sub>2.5</sub> bias  
 361 distribution patterns for two methods. From the boxplot, the average PM<sub>2.5</sub> bias of RF-  
 362 PMRS is close to zero (less than 5 μg/m<sup>3</sup>), which is greatly lower than that of PMRS.  
 363 Besides, PMRS PM<sub>2.5</sub> has a larger deviation range, which manifests in two aspects. One  
 364 is the maximum bias, specifically, it has exceeded 100 μg/m<sup>3</sup> at the BC site. The other  
 365 is the overall distribution of the data bias, the BJ site ones are mostly distributed below  
 366 zero, indicating an obvious overestimation. As for RF-PMRS, the above circumstances  
 367 are not obviously reflected in it. In addition, as can be seen from the indicators, RMSE  
 368 and MAE of RF-PMRS PM<sub>2.5</sub> decrease by about half in comparison with PMRS. And  
 369 the experiment has confirmed that the RF-PMRS PM<sub>2.5</sub> values have a strong linear  
 370 relationship with the ground truth at both sites, with R around 0.8 (0.82 at BJ and 0.78  
 371 at BC). Such a large optimization effect is attributed to the VE<sub>f</sub> expression replacement  
 372 to the fitted RF model.  
 373



374  
 375 **Fig. 6.** Boxplots of RF-PMRS (a) and PMRS (b) PM<sub>2.5</sub> bias at the BJ and BC sites. The upper (lower)



376 black line of each box represents the largest (smallest) value, the blue upper (lower) border  
 377 represents the upper (lower) quartile, and the red line denotes the median. Besides, the yellow,  
 378 orange, and gray symbols are the MB, RMSE, and MAE of the corresponding PM<sub>2.5</sub> concentration.  
 379

### 380 4.3. Generalization performance of RF-PMRS

381 Then, we estimate PM<sub>2.5</sub> based on PMRS and RF-PMRS within North China in 2017  
 382 (Fig. 1 exhibits the distribution pattern of the validation stations). Table 4 shows the  
 383 accuracy statistics. It can be seen that RF-PMRS greatly reduces the bias (about  
 384 44.87%), with MB of about 2.31 µg/m<sup>3</sup>. Similar to the results at the sites, the RF-PMRS  
 385 method can derive PM<sub>2.5</sub> concentration with practically no overestimation  
 386 (underestimation). Although there is not much difference in R values of the two models  
 387 (R of RF-PMRS is only improved by 0.01), RMSE and MAE of which decrease by  
 388 about 39.96 µg/m<sup>3</sup> and 18.86 µg/m<sup>3</sup>, respectively. As a result, the optimized method  
 389 deserves to be considered excellent.

390

391 **Table 4.** Validation results of PMRS and RF-PMRS PM<sub>2.5</sub> in North China.

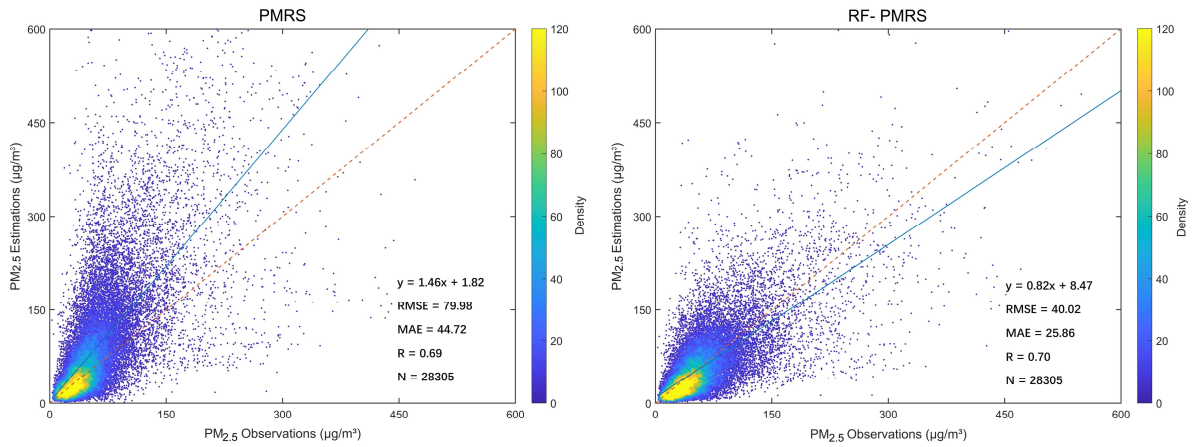
Method	R	MB (µg/m <sup>3</sup> )	RMB (%)	RMSE (µg/m <sup>3</sup> )	MAE (µg/m <sup>3</sup> )
PMRS	0.69	-29.34	48.71%	79.98	44.72
RF-PMRS	0.70	2.31	3.84%	40.02	25.86

392

393 Meanwhile, PM<sub>2.5</sub> scatterplots are presented below. As depicted in Fig. 7, there are  
 394 sufficient estimated samples (28305) in the NC region, which guarantees the credibility  
 395 of our validation results. In general, the RF-PMRS PM<sub>2.5</sub> values are distributed around  
 396 the 1:1 reference line evenly, with a slightly higher R of 0.70 compared to that of the  
 397 original method. And the slope of the linear fitting relationship reaches 0.82, which  
 398 indicates that the proposed method greatly reduces the overestimation of PMRS with a  
 399 linear slope of 1.46. Although the overall performance of the RF-PMRS estimations  
 400 maintains an excellent level, defects do remain. To be specific, in areas with high PM<sub>2.5</sub>  
 401 concentration (especially greater than 150 µg/m<sup>3</sup>), RF-PMRS results exist a slight  
 402 underestimation. It may be caused by the relatively small number of high-value PM<sub>2.5</sub>  
 403 points (only 1319 out of 28305), which is difficult to adequately reflect the fitting effect

404 of the method.

405



406

407 **Fig. 7.** Validation scatterplots of PM<sub>2.5</sub> results from PMRS (left) and RF-PMRS (right). Red dashed  
408 lines are 1:1 reference lines, and blue solid lines stand for the linear fits. The right legends show the  
409 point densities (frequency) represented by different colors.

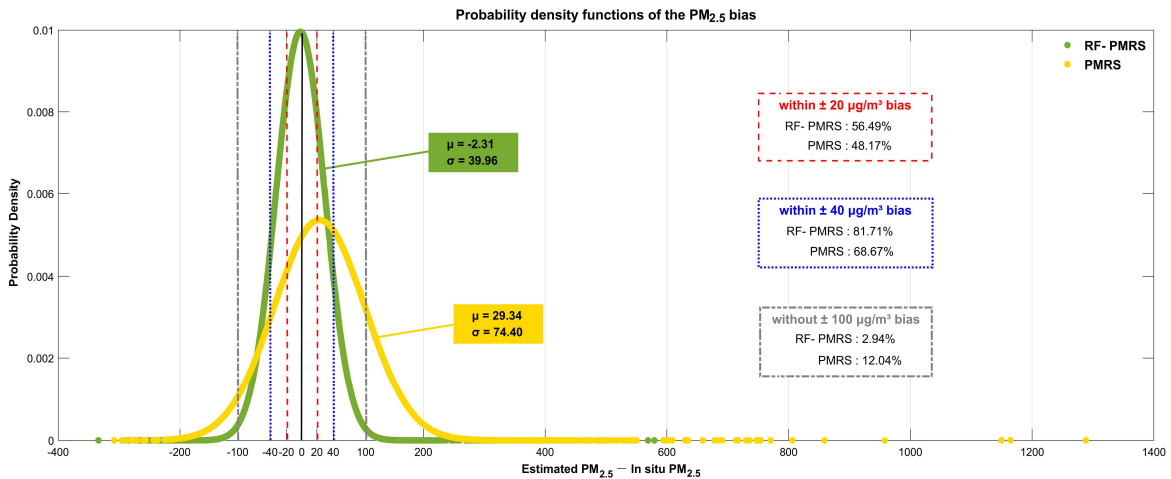
410

411 As for RF-PMRS, the deviation is reduced to a large extent, so the probability density  
412 function maps based on the bias of PMRS and RF-PMRS are further drawn. Fig. 8  
413 visualizes the probability densities within different bias ranges. In terms of distribution  
414 characteristics, the overall bias of RF-PMRS from the zero value (black solid line) is  
415 small. About the curve shape, it is high and narrow, manifesting that the bias has a lower  
416 standard deviation (STD) and is more prone to appear around the mean. However,  
417 PRMS shows a more discrete distribution pattern, and there are many outliers outside  
418 the range of greater than 600 µg/m<sup>3</sup>. Simultaneously, as can be concluded from the three  
419 boxes, within the bias range of ±20 µg/m<sup>3</sup> and ±40 µg/m<sup>3</sup>, the data numbers of RF-  
420 PMRS results increase by 8.32% and 12.81%, respectively. Outside the range of ±100  
421 µg/m<sup>3</sup>, the number decreases by 9.10%. Therefore, as far as the accuracy is concerned,  
422 RF-PMRS results have lower bias and better stability.

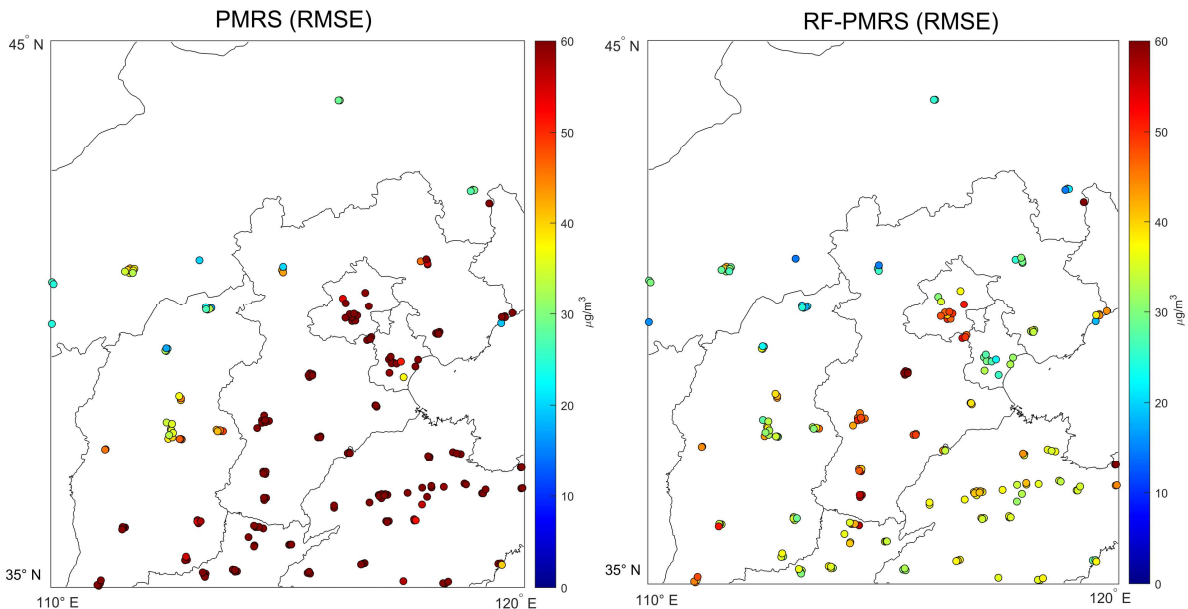
423

424 In addition to the above general performance comparison in Section 4.3, Fig. 9  
425 presents the annual average RMSE spatial distribution of PMRS and RF-PMRS PM<sub>2.5</sub>  
426 at NC stations. The two methods show a large deviation in the middle and southeast,  
427 and the RMSE map of PMRS has more red points. However, RF-PMRS can weaken

428 this phenomenon very well since its RMSE representative colors are generally light. In  
 429 particular, the proportion of dark red sites (RMSE greater than  $60 \mu\text{g}/\text{m}^3$ ) decreases  
 430 from 65.44% (PMRS) to 4.15% (RF-PMRS). In the areas where the ground stations are  
 431 clustered, the deviation also reduces significantly.  
 432



433 **Fig. 8.** Probability density functions of PMRS (yellow) and RF-PMRS (green)  $\text{PM}_{2.5}$  bias. The red,  
 434 blue and grey dotted lines indicate the bias boundaries of  $\pm 20 \mu\text{g}/\text{m}^3$ ,  $\pm 40 \mu\text{g}/\text{m}^3$ , and  $\pm 100 \mu\text{g}/\text{m}^3$ ,  
 435 respectively.  $\mu$  and  $\sigma$  represent the mean value and standard deviation of each data.  
 436  
 437



438 **Fig. 9.** RMSE of the year-average  $\text{PM}_{2.5}$  concentration values between different models and ground  
 439 stations (left: PMRS  $\text{PM}_{2.5}$ , right: RF-PMRS  $\text{PM}_{2.5}$ ). Note that the top red of the RMSE legend  
 440 indicates RMSE values equal to or greater than  $60 \mu\text{g}/\text{m}^3$ .  
 441  
 442

443 In a word, the above analysis demonstrates that compared with the simple quadratic  
 444 polynomial relationship (equation (10)), the established RF model in RF-PMRS can  
 445 more accurately capture the relationship between  $VE_f$  and multiple variables, thereby  
 446 improving the  $PM_{2.5}$  estimation accuracy.

447

## 448 **5. Discussion**

### 449 **5.1. Accuracy comparison of PMRS using MODIS/Phy-DL FMF**

450 To confirm the superiority of the Phy-DL FMF data adopted in our method  
 451 framework, taking the BJ and BC sites as examples (in 2017), the experiment compares  
 452 the  $PM_{2.5}$  accuracy and the number of effective days calculated by PMRS based on  
 453 different FMF. Table 5 presents the overall day-level results. Here, ‘DOY’ means the  
 454 day of the year and ‘valid’ means that all variables related to the  $PM_{2.5}$  calculation are  
 455 valid. As can be seen, after the FMF replacement, the valid DOY turns out to become  
 456 more (an increase of 113 days), which illustrates that the number of effective  $PM_{2.5}$   
 457 concentrations has gone up by about 5 times. Moreover, the accuracy has been  
 458 significantly enhanced, with R increased by about 0.30, RMSE and MAE decreased by  
 459 26.14% and 16.47% accordingly. On the whole, Phy-DL FMF contributes to the  
 460 improvement of PMRS results, signifying the first step optimization of the proposed  
 461 RF-PMRS method is effective.

462

463 **Table 5.** Validation results of the PMRS method using different FMF data. The valid DOY refers to  
 464 the number of days that the AOD, FMF, and other data are not missing when calculating  $PM_{2.5}$ . Note  
 465 that since the valid days of the two schemes are different, the MB and RMB are not compared.

	<b>Valid DOY</b>	<b>R</b>	<b>RMSE (<math>\mu\text{g}/\text{m}^3</math>)</b>	<b>MAE (<math>\mu\text{g}/\text{m}^3</math>)</b>
<b>PMRS with MODIS FMF</b>	30	0.38	63.01	35.64
<b>PMRS with Phy-DL FMF</b>	143	0.68	46.54	29.77

466

### 467 **5.2. Performance compared with other ML models**

468 Different machine learning models are suitable for diverse research data, and  
 469 decision tree (DT) models can better fit experiments with fewer variables, such as this  
 470 study. For comparison, except for RF, the Extremely Randomized Tree (ERT) (Geurts

471 et al., 2006) and Gradient Boosting Decision Tree (GBDT) (Friedman, 2001) models  
 472 have also been established. The results of training  $VE_f$  based on the above three DT  
 473 models are presented in Table 6 and Table 7. By contrast, RF performs best in CV and  
 474 IV experiments, as indicated by the multiple accuracy indicators. Although ERT and  
 475 GBDT models are comparable to RF in some indicators, there exists a certain degree  
 476 of overfitting in the above two models, which is manifested in that their IV results are  
 477 clearly worse than their respective CV ones. Thus, the RF model is applied to our study.

478

479 **Table 6.** Cross-validation results in comparison of the decision tree models for training  $VE_f$ . N  
 480 represents the number of data, and  $VE_f$  has no unit.

CV results					
	R	RMSE	RPE	MAE	N
RF	0.974	0.076	0.330	0.034	6463
ERT	0.972	0.079	0.343	0.035	
GBDT	0.973	0.078	0.339	0.036	

481

482 **Table 7.** Isolated-validation results in comparison of the decision tree models for training  $VE_f$ . The  
 483 indicators are the same as those in Table 6.

IV results					
	R	RMSE	RPE	MAE	N
RF	0.975	0.067	0.299	0.037	814
ERT	0.967	0.076	0.340	0.042	
GBDT	0.969	0.074	0.331	0.040	

484

### 485 5.3. Feature importance of the embedded RF model

486 Additionally, the feature importance of RF is calculated to evaluate the contribution  
 487 of model predictors to  $VE_f$  simulation. Fig. B2 (in Appendix B) shows the results by  
 488 normalization (taking 100 as the total). Without a doubt, FMF accounts for the largest  
 489 proportion, about 76.4%, which is consistent with the analysis when selecting the  $VE_f$ -  
 490 related variables (see Section 3.2). The contribution of spatiotemporal variables is about  
 491 1/3 of FMF, which indirectly affirms the credibility of RF feature learning. Also, it  
 492 provides a basis for further uncertainty optimization of  $VE_f$  and  $PM_{2.5}$  accuracy.

493

## 494 **6. Conclusion**

495 Among various satellite remote sensing methods for PM<sub>2.5</sub> retrieval, the semi-  
496 empirical physical approach has strong physical significance and clear calculation steps  
497 and derives the PM<sub>2.5</sub> mass concentration independently of in situ observations.  
498 However, the parameters with the meaning of optical properties are difficult to express,  
499 which need to be optimized. Hence, the study proposes a method (RF-PMRS) that  
500 embeds machine learning in a physical model to obtain surface PM<sub>2.5</sub>: 1) Based on the  
501 PMRS method and select the Phy-DL FMF product with a combined mechanism; 2)  
502 Use the RF model to fit the parameter VE<sub>f</sub>, rather than a simple quadratic polynomial.  
503 In the point-to-surface validation, RF-PMRS shows great optimized performance.  
504 Experiments at two AERONET sites show that R reaches up to 0.8. And in North China,  
505 RMSE decreases by 39.95 µg/m<sup>3</sup> with a 44.87% reduction in relative deviation. In the  
506 future, we will further explore the combination of atmospheric mechanism and machine  
507 learning, then research the PM<sub>2.5</sub> retrieval methods with physical meaning and higher  
508 accuracy.  
509

## 510 **Appendix A: Supplementary description**

### 511 **A1. 10-fold cross-validation and isolated-validation**

512 The sample-based 10-fold cross-validation method is applied to test the fitting and  
513 predictive ability of our model. The original dataset is randomly divided into ten parts,  
514 nine of which are used as the training set for model fitting, and the remaining one is  
515 used for prediction, then the cross-validation process is repeated ten rounds until each  
516 data has been used as the test set.

517 At the same time, when verifying the RF-based VE<sub>f</sub> model, the dataset in the period  
518 that did not participate in the training in Table 1 is used for isolated-validation.

519

### 520 **A2. Statistical indicators**

521

$$R = \frac{\sum_{i=1}^m (y_i - \bar{y}) \sum_{i=1}^m (f_i - \bar{f})}{\sqrt{\sum_{i=1}^m (y_i - \bar{y})^2} \sqrt{\sum_{i=1}^m (f_i - \bar{f})^2}}$$

522

$$MB = \bar{y} - \bar{f}$$

523

$$RMB = \text{abs}\left(\frac{\bar{y} - \bar{f}}{\bar{y}}\right)$$

524

$$RMSE = \sqrt{\frac{1}{m} \sum_{i=1}^m (y_i - f_i)^2}$$

525

$$MAE = \frac{1}{m} \sum_{i=1}^m |y_i - f_i|$$

526

$$RPE = \frac{\sqrt{\frac{1}{m} \sum_{i=1}^m (y_i - f_i)^2}}{\bar{y}}$$

527 where  $m$  is the total number of observations,  $i$  is the number of measurements,  $y_i$  is the  
 528  $i$ -th observation,  $f_i$  is the corresponding estimation result. And  $\bar{y}$  and  $\bar{f}$  are the  
 529 averages of all observations and estimates, respectively.

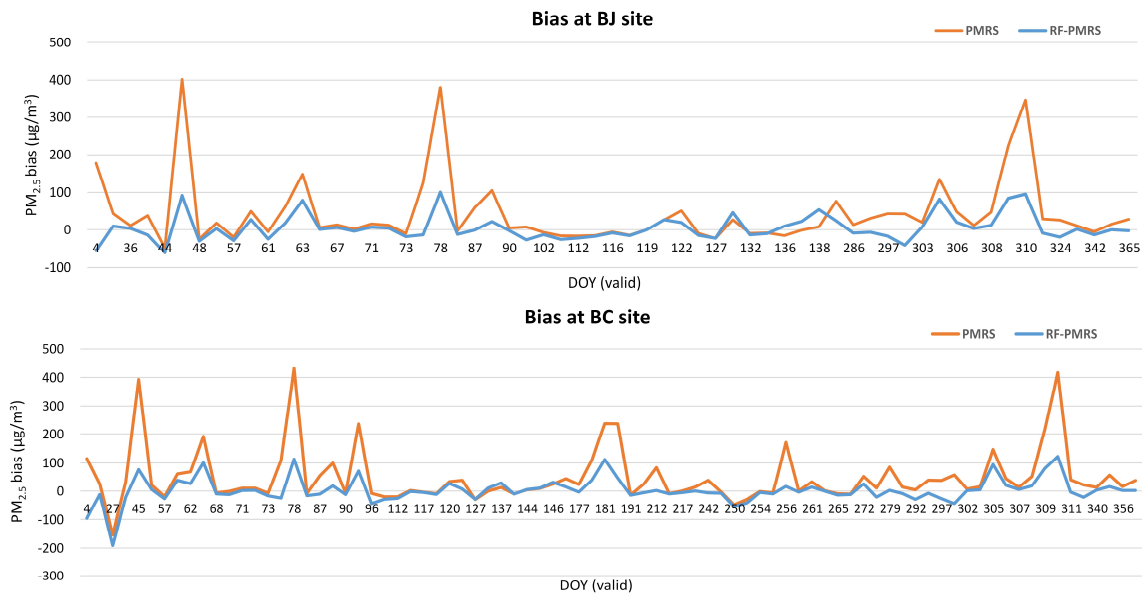
530

### 531 **A3. Parameter adjustments of the RF model**

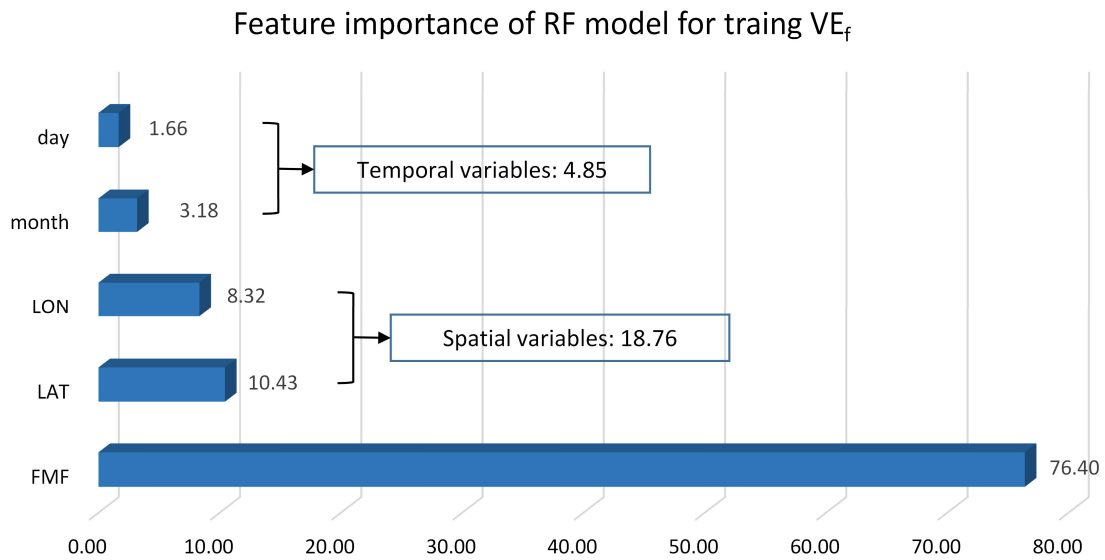
532 The four parameters of RF are adjusted, that is the correlation coefficient  $r$  changes  
 533 with (a) the number of trees, (b) maximum depth, (c) maximum number of features  
 534 when splitting, (d) minimum number of split samples. Experiments show that the  
 535 maximum depth varies greatly in a small range. To prevent overfitting, the four  
 536 parameters of RF are adjusted to 60, 10, 2, and 8. It can ensure high accuracy while  
 537 improving training efficiency.

538

539 **Appendix B: Figures**



540  
 541 **Fig. B1.** The time series of PMRS/RF-PMRS PM<sub>2.5</sub> bias at the Beijing and Beijing-CAMS sites  
 542 under their respective DOYs in 2017. The orange line represents the bias between the PM<sub>2.5</sub> values  
 543 of PMRS and stations, while the blue one indicates the PM<sub>2.5</sub> difference between RF-PMRS and  
 544 stations.  
 545



546  
 547 **Fig. B2.** The predictor importance results (normalized) of the RF model for training  $VE_f$ .  
 548

549 **Code and data availability**

550 All relevant codes as well as the intermediate data of this work are archived at  
 551 <https://doi.org/10.5281/zenodo.7183822> (Jin, 2022). The MCD19A2 data can be



552 downloaded on <https://ladsweb.modaps.eosdis.nasa.gov> (last access: 30-09-2022)  
553 (Lyapustin and Wang, 2015). Detailed information about the Phy-DL FMF dataset can  
554 be found at <https://doi.org/10.5281/zenodo.5105617> (Yan, 2021). Meteorological data  
555 used in this work are obtained at  
556 <https://cds.climate.copernicus.eu/cdsapp#!/dataset/reanalysis-era5-single-levels> (last  
557 access: 30-09-2022) (Hersbach et al., 2018). AERONET data was downloaded from  
558 <https://aeronet.gsfc.nasa.gov/> (last access: 30-09-2022) (Giles et al., 2019).

559

#### 560 **Author contributions**

561 **Caiyi Jin:** Data curation, Methodology, Formal analysis, Writing - original draft.  
562 **Qiangqiang Yuan:** Conceptualization, Supervision, Project administration, Writing -  
563 review and editing. **Tongwen Li:** Resources, Methodology, Writing - review and  
564 editing, Formal analysis. **Yuan Wang:** Methodology, Validation, Writing - review and  
565 editing. **Liangpei Zhang:** Supervision, Writing - review and editing.

566

#### 567 **Competing interests**

568 The contact author has declared that none of the authors has any competing interests.

569

#### 570 **Acknowledgments**

571 We gratefully acknowledge the Atmosphere Archive and Distribution System  
572 (LAADS), the ECMWF, the AERONET project, and the CNEMC for respectively  
573 providing the MODIS products, the meteorological data, the ground aerosol data, and  
574 the surface PM<sub>2.5</sub> concentration. We also thank other institutions which provide related  
575 data in this work.

576

#### 577 **Financial support**

578 This research was funded in part by the National Natural Science Foundation of  
579 China (No. 41922008 and No. 42201359), the Hubei Science Foundation for  
580 Distinguished Young Scholars (No. 2020CFA051) and the Guangdong Basic and  
581 Applied Basic Research Foundation (No. 2022A1515010492).

582

583 **References**

584 Belgiu, M., and Drăguț, L.: Random forest in remote sensing: A review of applications  
585 and future directions, *ISPRS J. Photogramm. Remote Sens.*, 114, 24-31,  
586 <https://doi.org/10.1016/j.isprsjprs.2016.01.011>, 2016.

587 Bowe, B., Xie, Y., Li, T., Yan, Y., Xian, H., and Al-Aly, Z.: The 2016 global and  
588 national burden of diabetes mellitus attributable to PM2.5 air pollution, *Lancet Planet.  
589 Health*, 2, e301-e312, [https://doi.org/10.1016/S2542-5196\(18\)30140-2](https://doi.org/10.1016/S2542-5196(18)30140-2), 2018.

590 Chen, X., de Leeuw, G., Arola, A., Liu, S., Liu, Y., Li, Z., and Zhang, K.: Joint retrieval  
591 of the aerosol fine mode fraction and optical depth using MODIS spectral reflectance  
592 over northern and eastern China: Artificial neural network method, *Remote Sens  
593 Environ*, 249, 112006, <https://doi.org/10.1016/j.rse.2020.112006>, 2020.

594 Friedman, J.H.: Greedy function approximation: a gradient boosting machine, *Ann Stat*,  
595 29(5), 1189–1232, <http://www.jstor.org/stable/2699986>, 2001.

596 Gao, J., Zhou, Y., Wang, J., Wang, T., and Wang, W.X.: Inter-comparison of WPSTM-  
597 TEOMTM-MOUDITM and investigation on particle density, *Huan Jing Ke Xue*, 28,  
598 1929-1934, <https://doi.org/10.3321/j.issn:0250-3301.2007.09.005>, 2007.

599 Gao, L., Li, J., Chen, L., Zhang, L., and Heidinger, A.K.: Retrieval and validation of  
600 atmospheric aerosol optical depth from AVHRR over China, *IEEE Trans Geosci  
601 Remote Sens*, 54, 6280-6291, <https://doi.org/10.1109/TGRS.2016.2574756>, 2016.

602 Geng, G., Zhang, Q., Martin, R.V., van Donkelaar, A., Huo, H., Che, H., Lin, J., and  
603 He, K.: Estimating long-term PM2.5 concentrations in China using satellite-based  
604 aerosol optical depth and a chemical transport model, *Remote Sens Environ*, 166, 262-  
605 270, <https://doi.org/10.1016/j.rse.2015.05.016>, 2015.

606 Geurts, P., Ernst, D., and Wehenkel, L.: Extremely randomized trees, *Mach Learn*, 63,  
607 3-42, <https://doi.org/10.1007/s10994-006-6226-1>, 2006.

608 Giles, D.M., Holben, B.N., Eck, T.F., Smirnov, A., Sinyuk, A., Schafer, J., Sorokin,  
609 M.G., and Slutsker, I.: Aerosol robotic network (AERONET) version 3 aerosol optical  
610 depth and inversion products, in: American Geophysical Union (AGU) 98th Fall  
611 Meeting Abstracts, New Orleans, America, 11-15 December 2017, A11O-01, 2017.

612 Giles, D. M., Sinyuk, A., Sorokin, M. G., Schafer, J. S., Smirnov, A., Slutsker, I., Eck,  
613 T. F., Holben, B. N., Lewis, J. R., Campbell, J. R., Welton, E. J., Korkin, S. V., and  
614 Lyapustin, A. I.: Advancements in the Aerosol Robotic Network (AERONET) Version  
615 3 database - automated near-real-time quality control algorithm with improved cloud  
616 screening for Sun photometer aerosol optical depth (AOD) measurements, *Atmos Meas*  
617 *Tech*, 12, 169–209, <https://doi.org/10.5194/amt-12-169-2019>, 2019.

618 Gupta, P., and Christopher, S.A.: Particulate matter air quality assessment using  
619 integrated surface, satellite, and meteorological products: Multiple regression approach,  
620 *J. Geophys. Res. Atmos.*, 114, D14205, <https://doi.org/10.1029/2008JD011496>, 2009.

621 Hand, J.L., and Kreidenweis, S.M.: A new method for retrieving particle refractive  
622 index and effective density from aerosol size distribution data, *Aerosol Sci Technol*, 36,  
623 1012-1026, <https://doi.org/10.1080/02786820290092276>, 2002.

624 Hänel, G., and Thudium, J.: Mean bulk densities of samples of dry atmospheric aerosol  
625 particles: A summary of measured data, *Pure Appl. Geophys.*, 115, 799-803,  
626 <https://doi.org/10.1007/BF00881211>, 1977.

627 He, J., Yuan, Q., Li, J., and Zhang, L.: PoNet: A universal physical optimization-based  
628 spectral super-resolution network for arbitrary multispectral images, *Inform Fusion*, 80,  
629 205-225, <https://doi.org/10.1016/j.inffus.2021.10.016>, 2022.

630 He, J., Li, J., Yuan, Q., Shen, H., and Zhang, L.: Spectral Response Function-Guided  
631 Deep Optimization-Driven Network for Spectral Super-Resolution, *IEEE Trans Neural*  
632 *Netw. Learn. Syst.*, PP(99), 1-15, <https://doi.org/10.1109/TNNLS.2021.3056181>, 2021.

633 Hersbach, H., Bell, B., Berrisford, P., Biavati, G., Horányi, A., Muñoz Sabater, J.,  
634 Nicolas, J., Peubey, C., Radu, R., Rozum, I., Schepers, D., Simmons, A., Soci, C., Dee,  
635 D., Thépaut, J.-N.: ERA5 hourly data on single levels from 1979 to present, Copernicus  
636 Climate Change Service (C3S) Climate Data Store (CDS) [data set], (Accessed on 30-  
637 09-2022), <https://doi.org/10.24381/cds.adbb2d47>, 2018.

638 Holben, B.N., Eck, T.F., Slutsker, I., Tanré, D., Buis, J.P., Setzer, A., Vermote, E.,  
639 Reagan, J.A., Kaufman, Y.J., Nakajima, T., Lavenu, F., Jankowiak, I., and Smirnov, A.:  
640 AERONET — A federated instrument network and data archive for aerosol

641 characterization, *Remote Sens Environ*, 66, 1-16, [https://doi.org/10.1016/S0034-](https://doi.org/10.1016/S0034-4257(98)00031-5)  
642 [4257\(98\)00031-5](https://doi.org/10.1016/S0034-4257(98)00031-5), 1998.

643 Irrgang, C., Boers, N., Sonnewald, M., Barnes, E.A., Kadow, C., Staneva, J., and  
644 Saynisch-Wagner, J.: Towards neural Earth system modelling by integrating artificial  
645 intelligence in Earth system science, *Nat. Mach. Intell.*, 3, 667-674,  
646 <https://doi.org/10.1038/s42256-021-00374-3>, 2021.

647 Jin, C.: An optimized semi-empirical physical approach for satellite-based PM2.5  
648 retrieval: using random forest model to simulate the complex parameter, Zenodo [code],  
649 <https://doi.org/10.5281/zenodo.7183822>, 2022.

650 Koelemeijer, R.B.A., Homan, C.D., and Matthijsen, J.: Comparison of spatial and  
651 temporal variations of aerosol optical thickness and particulate matter over Europe,  
652 *Atmospheric Environ.*, 40, 5304-5315, <https://doi.org/10.1016/j.atmosenv.2006.04.044>,  
653 2006.

654 Kokhanovsky, A.A., Prikhach, A.S., Katsev, I.L., and Zege, E.P.: Determination of  
655 particulate matter vertical columns using satellite observations, *Atmos Meas Tech*, 2,  
656 327-335, <https://doi.org/10.5194/amt-2-327-2009>, 2009.

657 Lee, J.-B., Lee, J.-B., Koo, Y.-S., Kwon, H.-Y., Choi, M.-H., Park, H.-J., and Lee, D.-  
658 G.: Development of a deep neural network for predicting 6 h average PM2.5  
659 concentrations up to 2 subsequent days using various training data, *Geosci. Model Dev.*,  
660 15, 3797–3813, <https://doi.org/10.5194/gmd-15-3797-2022>, 2022.

661 Li, T., Shen, H., Zeng, C., Yuan, Q., and Zhang, L.: Point-surface fusion of station  
662 measurements and satellite observations for mapping PM2.5 distribution in China:  
663 Methods and assessment, *Atmospheric Environ.*, 152, 477-489,  
664 <https://doi.org/10.1016/j.atmosenv.2017.01.004>, 2017.

665 Li, Z., Zhang, Y., Shao, J., Li, B., Hong, J., Liu, D., Li, D., Wei, P., Li, W., Li, L.,  
666 Zhang, F., Guo, J., Deng, Q., Wang, B., Cui, C., Zhang, W., Wang, Z., Lv, Y., Xu, H.,  
667 Chen, X., Li, L., and Qie, L.: Remote sensing of atmospheric particulate mass of dry  
668 PM2.5 near the ground: Method validation using ground-based measurements, *Remote*  
669 *Sens Environ*, 173, 59-68, <https://doi.org/10.1016/j.rse.2015.11.019>, 2016.

670 Lyapustin, A., Wang, Y., Laszlo, I., Kahn, R., Korkin, S., Remer, L., Levy, R., and

671 Reid, J.S.: Multiangle implementation of atmospheric correction (MAIAC): 2. Aerosol  
672 algorithm, *J. Geophys. Res. Atmos.*, 116, D03211,  
673 <https://doi.org/10.1029/2010JD014986>, 2011.

674 Lyapustin, A., Wang, Y., Xiong, X., Meister, G., Platnick, S., Levy, R., Franz, B.,  
675 Korkin, S., Hilker, T., Tucker, J., Hall, F., Sellers, P., Wu, A., and Angal, A.: Scientific  
676 impact of MODIS C5 calibration degradation and C6+ improvements, *Atmos Meas  
677 Tech*, 7, 4353-4365, <https://doi.org/10.5194/amt-7-4353-2014>, 2014.

678 Lyapustin, A., and Wang, Y.: MCD19A2 MODIS/Terra+Aqua Aerosol Optical  
679 Thickness Daily L2G Global 1km SIN Grid, NASA LP DAAC [data set], (Accessed  
680 on 30-09-2022), <http://doi.org/10.5067/MODIS/MCD19A2.006>, 2015.

681 Lyu, B., Huang, R., Wang, X., Wang, W., and Hu, Y.: Deep-learning spatial principles  
682 from deterministic chemical transport models for chemical reanalysis: an application in  
683 China for PM<sub>2.5</sub>, *Geosci. Model Dev.*, 15, 1583–1594, [https://doi.org/10.5194/gmd-](https://doi.org/10.5194/gmd-15-1583-2022)  
684 [15-1583-2022](https://doi.org/10.5194/gmd-15-1583-2022), 2022.

685 Ma, Z., Hu, X., Huang, L., Bi, J., and Liu, Y.: Estimating ground-Level PM<sub>2.5</sub> in China  
686 using satellite remote sensing, *Environ. Sci. Technol.*, 48, 7436-7444,  
687 <https://doi.org/10.1021/es5009399>, 2014.

688 Pope III, C.A., Burnett, R.T., Thun, M.J., Calle, E.E., Krewski, D., Ito, K., and Thurston,  
689 G.D.: Lung cancer, cardiopulmonary mortality, and long-term exposure to fine  
690 particulate air pollution, *JAMA*, 287, 1132-1141,  
691 <https://doi.org/10.1001/jama.287.9.1132>, 2002.

692 Raut, J., and Chazette, P.: Assessment of vertically-resolved PM<sub>10</sub> from mobile lidar  
693 observations, *Atmospheric Chem. Phys.*, 9, 8617-8638, [https://doi.org/10.5194/acp-9-](https://doi.org/10.5194/acp-9-8617-2009)  
694 [8617-2009](https://doi.org/10.5194/acp-9-8617-2009), 2009.

695 Rodriguez, J.D., Perez, A., and Lozano, J.A.: Sensitivity analysis of k-fold cross  
696 validation in prediction error estimation, *IEEE Trans. Pattern Anal. Mach. Intell.*, 32,  
697 569-575, <https://doi.org/10.1109/TPAMI.2009.187>, 2009.

698 Shi, X., Zhao, C., Jiang, J.H., Wang, C., Yang, X., and Yung, Y.L.: Spatial  
699 representativeness of PM<sub>2.5</sub> concentrations obtained using observations from network  
700 stations, *J. Geophys. Res. Atmos.*, 123, 3145-3158,

701 <https://doi.org/10.1002/2017JD027913>, 2018.

702 Simmons, A.J., Untch, A., Jakob, C., Källberg, P., and Undén, P.: Stratospheric water  
703 vapour and tropical tropopause temperatures in ECMWF analyses and multi-year  
704 simulations, *Q J R Meteorol Soc*, 125, 353-386,  
705 <https://doi.org/10.1002/qj.49712555318>, 1999.

706 Svetnik, V., Liaw, A., Tong, C., Culberson J.C., Sheridan R.P., and Feuston, B.P.:  
707 Random Forest: A Classification and Regression Tool for Compound Classification  
708 and QSAR Modeling, *J. Chem. Inf. Comput. Sci.*, 43, 6, 1947-1958,  
709 <https://doi.org/10.1021/ci034160g>, 2003.

710 Van Donkelaar, A., Martin, R.V., and Park, R.J.: Estimating ground-level PM<sub>2.5</sub> using  
711 aerosol optical depth determined from satellite remote sensing, *J. Geophys. Res. Atmos.*,  
712 111, D21201, <https://doi.org/10.1029/2005JD006996>, 2006.

713 Wang, Y., Yuan, Q., Li, T., Shen, H., Zheng, L., and Zhang, L.: Evaluation and  
714 comparison of MODIS Collection 6.1 aerosol optical depth against AERONET over  
715 regions in China with multifarious underlying surfaces, *Atmospheric Environ.*, 200,  
716 280-301, <https://doi.org/10.1016/j.atmosenv.2018.12.023>, 2019.

717 Wu, X., Wang, Y., He, S., and Wu, Z.: PM<sub>2.5</sub> / PM<sub>10</sub> ratio prediction based on a long  
718 short-term memory neural network in Wuhan, China, *Geosci. Model Dev.*, 13, 1499–  
719 1511, <https://doi.org/10.5194/gmd-13-1499-2020>, 2020.

720 Xu, P., Chen, Y., and Ye, X.: Haze, air pollution, and health in China, *Lancet*, 382,  
721 2067, [https://doi.org/10.1016/S0140-6736\(13\)62693-8](https://doi.org/10.1016/S0140-6736(13)62693-8), 2013.

722 Yan, X., Zang, Z., Li, Z., Luo, N., Zuo, C., Jiang, Y., Li, D., Guo, Y., Zhao, W., Shi,  
723 W., and Cribb, M.: A global land aerosol fine-mode fraction dataset (2001--2020)  
724 retrieved from MODIS using hybrid physical and deep learning approaches, *Earth Syst.*  
725 *Sci. Data*, 14, 1193-1213, <https://doi.org/10.5194/essd-14-1193-2022>, 2022.

726 Yan, X., Li, Z., Shi, W., Luo, N., Wu, T., and Zhao, W.: An improved algorithm for  
727 retrieving the fine-mode fraction of aerosol optical thickness, part 1: Algorithm  
728 development, *Remote Sensing of Environment*, 192, 87-97,  
729 <https://doi.org/10.1016/j.rse.2017.02.005>, 2017.

730 Yan, X.: Physical and deep learning retrieved fine mode fraction (Phy-DL FMF),  
731 Zenodo [data set], (Accessed on 30-09-2022), <https://doi.org/10.5281/zenodo.5105617>,  
732 2021.

733 Yang, Q., Yuan, Q., Li, T., and Yue, L.: Mapping PM2.5 concentration at high  
734 resolution using a cascade random forest based downscaling model: Evaluation and  
735 application, *J. Clean. Prod.*, 277, 123887,  
736 <https://doi.org/10.1016/j.jclepro.2020.123887>, 2020.

737 Yuan, Q., Shen, H., Li, T., Li, Z., Li, S., Jiang, Y., Xu, H., Tan, W., Yang, Q., Wang,  
738 J., Gao, J., and Zhang, L.: Deep learning in environmental remote sensing:  
739 Achievements and challenges, *Remote Sens Environ*, 241, 111716,  
740 <https://doi.org/10.1016/j.rse.2020.111716>, 2020.

741 Zhang, Y., Li, Z., Bai, K., Wei, Y., Xie, Y., Zhang, Y., Ou, Y., Cohen, J., Zhang, Y.,  
742 Peng, Z., Zhang, X., Chen, C., Hong, J., Xu, H., Guang, J., Lv, Y., Li, K., and Li, D.:  
743 Satellite remote sensing of atmospheric particulate matter mass concentration:  
744 Advances, challenges, and perspectives, *Fundamental Research*, 1, 240-258,  
745 <https://doi.org/10.1016/j.fmre.2021.04.007>, 2021.

746 Zhang, Y., Li, Z., Chang, W., Zhang, Y., de Leeuw, G., and Schauer, J.J.: Satellite  
747 observations of PM2.5 changes and driving factors based forecasting over China 2000–  
748 2025, *Remote Sens.*, 12(16), 2518, <https://doi.org/10.3390/rs12162518>, 2020.

749 Zhang, Y., and Li, Z.: Remote sensing of atmospheric fine particulate matter (PM2.5)  
750 mass concentration near the ground from satellite observation, *Remote Sens Environ*,  
751 160, 252-262, <https://doi.org/10.1016/j.rse.2015.02.005>, 2015.